Joint Classification of Hyperspectral and Multispectral Images for Mapping Coastal Wetlands

Chang Liu, *Student Member, IEEE*, Ran Tao ⓘ, *Senior Member, IEEE*, Wei Li ⓘ, *Senior Member, IEEE*, Mengmeng Zhang ⓘ, *Member, IEEE*, Weiwei Sun ⓘ, *Senior Member, IEEE*, and Qian Du ⓘ, *Fellow, IEEE*

Abstract—It is significant for restoration and protection of natural resources and ecological services in coastal wetlands to map different land cover types with satellite remote sensing data. Considering difficulties of wetland species classification, hyperspectral images (HSIs) with high spectral resolution and multispectral images (MSI) with high spatial resolution are considered to achieve complementary advantages of multisource data. An effective approach, named as multistream convolutional neural network, is proposed to achieve fine classification of coastal wetlands. First, regression processing is adopted to make chaotically scattered coastal wetland data more compact and different. Second, through appropriate feature extraction and feature fusion strategies, high-level information of multisource data in regression domain is fused to distinguish different land cover. Experiments on GF-5 HSIs and Sentinel-2 MSIs are carried out in order to validate the classification performance of the proposed approach in two coastal wetlands of research value in China, i.e., Yellow River Estuary and Yancheng coastal wetland. Experimental results demonstrate the effectiveness of the proposed method compared with the state-of-the-art methods in the field, especially when the number of sample size is extremely small.

Index Terms—Coastal wetlands, convolutional neural network (CNN), data fusion, hyperspectral imagery (HSI), least squares regression (LSR), multispectral imagery (MSI).

I. INTRODUCTION

WETLANDS, distributed in all climate zones ranging from the tropics to the tundra [1], are among the most productive and valuable ecosystems in the world [2]. The total value of services provided by global wetland ecosystems is nearly half of the total value of services that global ecosystems provide [3]. Unfortunately, global sea-level rise [4], [5] and inappropriate anthropogenic activities lead to the dramatic

Chang Liu, Ran Tao, Wei Li, and Mengmeng Zhang are with the School of Information and Electronics, Beijing Institute of Technology, Beijing 100081, China (e-mail: 2929166864@qq.com; rantao@bit.edu.cn; leewei36@gmail.com; 7520200002@bit.edu.cn).

Weiwei Sun is with the Department of Geography and Spatial Information Techniques, Ningbo University, Ningbo 315211, China (e-mail: nbsww@outlook.com).

Qian Du is with the Department of Electrical and Computer Engineering, Mississippi State University, Starkville, MS 39762 USA (e-mail: du@ece.msstate.edu).

Digital Object Identifier 10.1109/JSTARS.2020.3040305

degradation in the area of coverage, ecological value, and biodiversity in the worldwide coastal wetlands over the past decades. Thus, detailed information about wetland vegetation types and their spatial distribution in relation to topographic and hydrographic features need to be assessed [6]. Classification of coastal wetlands is a challenging task, due to their complicated composition and pattern [7]. High-quality remote sensing data is an important tool for rapid wetland assessment and proactive management [8], because of its unique characteristics in an easy data acquisition, spatially continuous coverage, and short revisiting periods [9]. In this case, multispectral remote sensing images with high spatial resolution have the potential ability to classify wetland types [2]. However, it is difficult to classify the types of coastal wetlands with various spectral features similar to vegetation. Hyperspectral images (HSIs) have a wide spectral range and high spectral resolution [10], [11]. Therefore, they can help separate coastal wetland species with similar spectral features. However, most of coastal wetland plants are mixed and marshy, and the spatial resolution of HSI is low; it is difficult for HSI distinguish vegetation types [12]. Multispectral images (MSIs) are collected with high spatial resolution to provide more spatial contexture details [2], [13]. Therefore, the fusion of HSI and MSI can integrate diverse information and improve the performance of coastal wetlands mapping.

Divergences in spectral characteristics within HSI and MSI can reflect different ground objects [14]. MSIs are the most common images used in coastal wetlands [2], [15]. In previous studies, Landsat MSS, Landsat TM, Landsat ETM+, SPOT, and Sentinel-2 images have predominantly formed the basis of remote sensing techniques used for coastal wetlands monitoring and for land cover mapping, extraction, and classification [16]–[19]. Supervised classifiers are usually employed to make the pixel-based classification on spectral signatures, for example, machine learning like support vector machine (SVM) [20] and random forest (RF) [21]. Reschke and Hüttich combined multitemporal Landsat imagery with high-resolution satellite data and adopted the RF algorithm to extract subpixel information of coastal wetland classes [22]. Pierre *et al.* investigated the potential of optical remote sensing images for mapping the primary vegetation groups in the Dabus Wetlands using the nonparametric RF classifier [23].

High spectral resolution (<10 nm) of HSI reflects greater potentials in identifying different ground objects of coastal wetlands with subtle spectral divergence [24], [25]. In recent years, HSI research has received extensive attention [26]–[29]. Some

hyperspectral sensors have been utilized in mapping coastal wetlands, e.g., Earth Observing-1 (EO-1) Hyperion, Hyperspectral InfraRed Image, Compact High Resolution Imaging Spectrometer, and Hyperspectral Imager for the Coastal Ocean [10], [30]–[34]. Zomer *et al.* [8] used prosted-1 airborne hyperspectral data (5-m resolution, 128 bands) and wetland spectrum library to classify vegetation in Pacheco Creek wetland in California, demonstrating that advanced sensors have unparalleled advantages in wetland vegetation classification and mapping. Jiao *et al.* proposed a hierarchical classification framework that implemented two levels of classification scheme to identify different land cover types of coastal wetlands and verified that GF-5 data are superior to Landsat-8 and Sentinel-2 multispectral data in obtaining fine classification results of coastal wetlands [12]. Deep learning methods incorporating both spectral and spatial information have been improved classification accuracy. Contextual deep convolutional neural network (CD-CNN) jointly exploited local spatial–spectral relationships of neighboring pixel vectors within a square window to obtain contextual interactions [35]. Besides, there are some latest spectral image classification methods, such as collaborative learning, ensemble learning, and graph convolutional networks, which effectively improve the classification accuracy [36]–[38]. However, pixel-based classification performance is always limited for complicated landscape with diverse land cover types and their small patch sizes [39]. Moreover, spectral variations cause different species to have similar spectral signatures [40]. Single source of spectral information may not distinguish mixed species composition of wetlands and often leads to low mapping accuracies.

Fusion of multisource images can overcome the shortage of single remote sensing image data source [41]. By taking into account temporal, spectral, and spatial resolution of different remote sensing images, advantages of multiple data sources can be gathered to achieve better classification performance [42]–[48]. Amani *et al.* [45] classified a wetland in Newfoundland, Canada, by using four spectral indexes of different data types, including RapidEye, Sentinel 2A, ASTER, and Landsat 8, and made fully use of texture features and proportion features of each data. Jahncke *et al.* [46] used RADARSAT-2, polSAR, LiDAR, and QuickBird multisource remote sensing data to divide a wetland in Nova Scotia, Canada, into five types. Specifically, the CNN algorithm has also been successfully used for multisource remote sensing fusion classification in various applications. A two-branch CNN adopted the feature fusion method to fuse HSI and LiDAR or high-resolution visible-band image, which effectively combined the advantages of images from different sensors [47]. Zhao *et al.* used hierarchical random walk and deep CNN architecture to jointly classify HSI and LiDAR data [48]. Nonetheless, fine-scale representation of wetland plant species has proved to be challenging because of high level of spectral confusion between species [49]–[52]. Additionally, wetlands exhibit high spectral and spatial variability, which can also complicate mapping of wetland vegetation [53], [54]. Existing methods cannot specifically solve the problems in coastal wetlands, and the existing fusion strategies cannot increase mapping reliability.

In view of the challenges mentioned above, a coastal wetland joint classification method, multistream CNN, is proposed based on multisource remote sensing data fusion. The first part is to learn a more compact and discriminative regression transformation from the training dataset to solve the problems of small spectral difference of wetland vegetation and different spectral characteristics of the same ground object. Interclass sparsity-based discriminative least squares regression (ICS_DLSR) [55] is used to reduce the margin of intraclass and simultaneously enlarge the margin of interclass for better classification performance. The second part is regression data feature extraction network. The spatial and spectral features of regression data are extracted according to the characteristics of HSI and MSI. The two-branch CNN is used to extract spatial and spectral information in HSI, and a cascade network is utilized to process spatial information in MSI. Finally, the above features are stacked for joint classification. Meanwhile, the proposed method has good universality. Satisfied classification has been verified in the HSI and MSI of Yellow River Estuary and Yancheng coastal wetland taken by GF-5 satellite and Sentinel-2 in China.

The main contributions of this article are as follows.

1) Joint classification of multisource remote sensing images is designed for coastal wetland mapping. A spatial–spectral two-stream CNN feature extractor is employed to extract high-resolution spectral and spatial features of HSI, and high-resolution spatial features of MSI are extracted to make up for the shortage of HSI.
2) An effective regression method ICS_DLSR is employed to remote sensing data of coastal wetlands. This is especially important in practice where intraclass differences and interclass similarities exist in optical remote sensing data of coastal wetlands.
3) An appropriate feature extraction strategy and a fusion strategy are developed to fuse high-level features from spatial information of MSI and spectral and spatial information of HSI, which can significantly improve the accuracy of coastal wetlands classification.

The rest of this article is organized as follows. Section II reviews the ISC_DLSR and the two-branch CNN. Section III introduces the proposed method. Section IV demonstrates the experiment results in two experimental areas. Section V concludes this article.

II. RELATED WORKS

A. ICS_DLSR

Compared with conventional subspace learning methods, the least squares regression (LSR) method is more favorable since it is flexible to introduce various meaningful regularizations to improve their interpretability and performances [56].

Let $X = [x_1, x_2, \ldots, x_n] \in R^{m \times n}$ be the training set with n training samples from c classes, where m is the feature dimension of each sample. Let a zero–one matrix $Y = [y_1, y_2, \ldots, y_n] \in R^{c \times n}$ represent the label matrix corresponding to the training set X. Standard LR (StLR) aims at jointly learning a projection that can well transform the given training samples into their

respective class labels as follows:

$$\min_{Q}\|Y - QX\|_F^2 + \lambda\|Q\|_F^2 \tag{1}$$

where $Q \in R^{c \times m}$ is the transformation matrix and λ is the regularization parameter with a small positive value. However, it only focuses on fitting the input features to the corresponding output labels while ignoring the correlations among samples. Moreover, the used label matrix, i.e., zero–one label matrix, is inappropriate for classification.

ICS_DLSR [55] does not focus on preserving the structure of data, but intends to make the transformed samples of the same class to have a common sparsity structure. For this goal, an interclass sparsity constraint is introduced to the StLR regression model such that the margins of samples from the same class can be greatly reduced, while those of samples from different classes can be enlarged. In addition, an error term with a row-sparsity constraint is introduced to relax the strict zero–one label matrix, which allows the method to be more flexible in learning the discriminative transformation matrix. The regression model of ICS_DLSR is formulated as follows:

$$\min_{Q,E} \frac{1}{2}\|Y + E - QX\|_F^2 + \frac{\lambda_1}{2}\|Q\|_F^2$$
$$+ \lambda_2 \sum_{i=1}^{c}\|QX_i\|_{2,1} + \lambda_3\|E\|_{2,1} \tag{2}$$

where E denotes the errors and λ_1, λ_2, and λ_3 are regularization parameters. Different from the StLR, $\frac{\lambda_1}{2}\|Q\|_F^2$ is a novel class sparsity constraint, which was introduced into the StLR to make the transformed samples of the same class have the common sparsity structure. Considering that the zero–one label matrix Y is too strict and inappropriate for classification, we introduce a sparsity error term $\lambda_3\|E\|_{2,1}$ to relax it. The alternating direction method is adopted to solve this optimization equation [55], [57], [58]. It has been shown that ICS_DLSR performs better than other methods for multiclass classification.

B. Two-Branch CNN

CNN-based spectral–spatial feature extraction and classification can be generally divided into two categories. The first category extracts joint spectral–spatial features using 3-D filtering [59], [60]. The second category extracts spectral and spatial features separately and fuses them subsequently [47], [48], [61]. 3-D CNN feature extraction and classification methods often exploit shallow networks to avoid overfitting due to an additional filter in the spectral dimension compared to the 2-D CNN [60]. This limits their ability in exploiting the available spectral–spatial information, and the resulting classification maps tend to be oversmoothed.

The two-branch CNN model [47] contains two different branches, which focus on combining features extracted from HSI and other source data, such as LiDAR or visual images (VIS). For the HSI branch, a dual-tunnel CNN is used for the spectral–spatial feature extraction on the local HSI patch. More specifically, a pure 2-D CNN is utilized to focus spatial

information in the local patch windows, and a 1-D CNN is employed for spectral feature of the center pixel.

The spectral tunnel concentrates on the center pixel $\mathbf{H}_{i,j}^{\mathrm{spec}}$ at the location $p_{i,j}$, which only makes up of simple operations, including 1-D convolution layer, activation, max-pooling, and batch normalization [62], and the output spectral features $\mathbf{F}_{i,j}^{\mathrm{spec}}$ are then flatten. The spatial tunnel takes a patch centered at the pixel $p_{i,j}$ with a radius r as input data. The raw data patch $\mathbf{H}_{i,j}^{\mathrm{spat}} \in R^{ksize \times ksize}(ksize = 2 \times r + 1)$ is fed into the 2-D CNN tunnel with the same architecture as the spectral tunnel. The 2-D convolution and batch normalization carry out the spatial features $\mathbf{F}_{i,j}^{\mathrm{spat}}$ from the center target $p_{i,j}$ surrounding domain. The spatial–spectral features are then subsequently fused in the fully connected layer through concatenation or stacking and the output of the full connection layer can be expressed as

$$\mathbf{F}_{i,j}^{\mathrm{spec} \oplus \mathrm{spat}} = f(W \times (\mathbf{F}_{i,j}^{\mathrm{spec}}\|\mathbf{F}_{i,j}^{\mathrm{spat}} + b)) \tag{3}$$

where W and b are the weights and bias of the full connection layer, respectively.

For the other branch, a cascade network [63], which passes multiscale features to output, is adopted to exploit spatial information. The cascade block is defined as

$$v_m = g_m(u_1, \{\mathbf{W}_i\}) + u_1 \tag{4}$$
$$v = g_s(u_s, \{\mathbf{W}_j\}) + u_s \tag{5}$$

where u and v are the input and output vectors of the cascade block, and $g_m(u_1, \{\mathbf{W}_i\})$ and $g_s(u_s, \{\mathbf{W}_j\})$ represent the function mapping operation between two corresponding shortcut paths. Inherited from the ResNet strategy, the cascade network is designed to combine different level features from unequal layers for feature reuse and propagation. Traditional residual building block does not fully utilize the middle layer information, but the cascade block catches multiple scales' information for more complete features.

III. PROPOSED JOINT CLASSIFICATION METHOD

A. Overall Architecture and Analysis

A method called multistream CNN based on ICS_DLSR and two-branch CNN is proposed. The main procedure of the proposed classification framework is shown in Fig. 1. ICS_DLSR regression transformation of coastal wetland data can effectively reduce the intraclass variations and alleviate interclass similarity in wetland species [64]. The spectral and spatial information fusion can effectively make up for the shortage of single source data [42], [43], [49], solving the problems of coastal wetlands categories complexity and sample imbalance for improved mapping accuracy.

Specifically, HSIs and MSIs are first transformed by ICS_DLSR, which maps the raw original domain data to more compact and discriminative domain. Because such a transform is only the mapping of the original data, spectral and spatial details of HSI in the regression domain are still retained. Then, the two-branch CNN, which has excellent performance in spatial and spectral information extraction, is employed. Two-branch
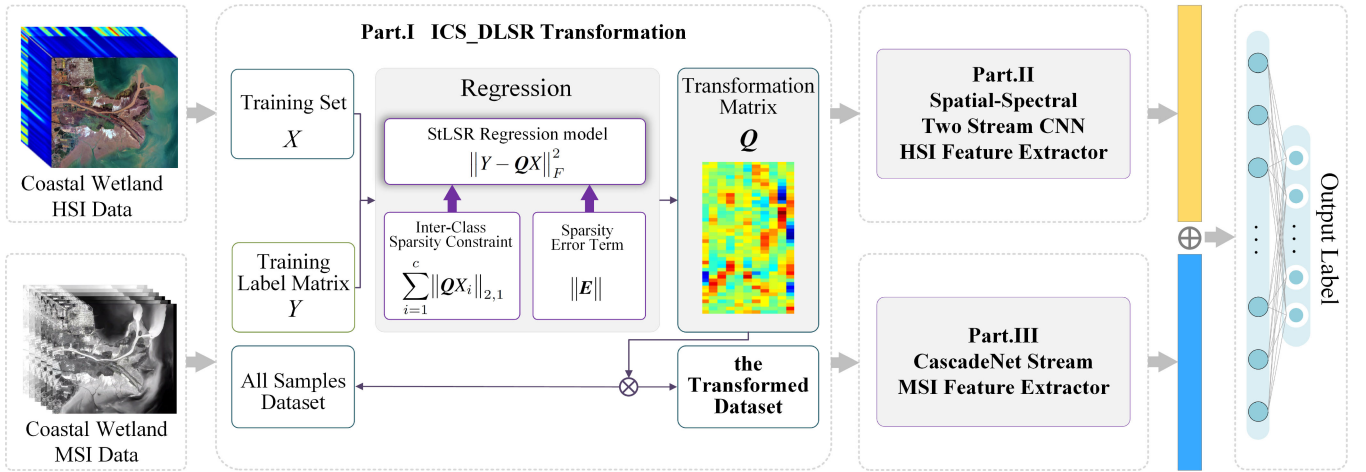
Fig. 1. Overall architecture of the proposed multistream CNN method. Part I denotes a standard LSR introduced an interclass sparsity constraint. Part II denotes a two-stream CNN for regression domain HSI spatial–spectral feature extractor. Part III denotes a CascadeNet for the regression domain MSI spatial feature extractor.
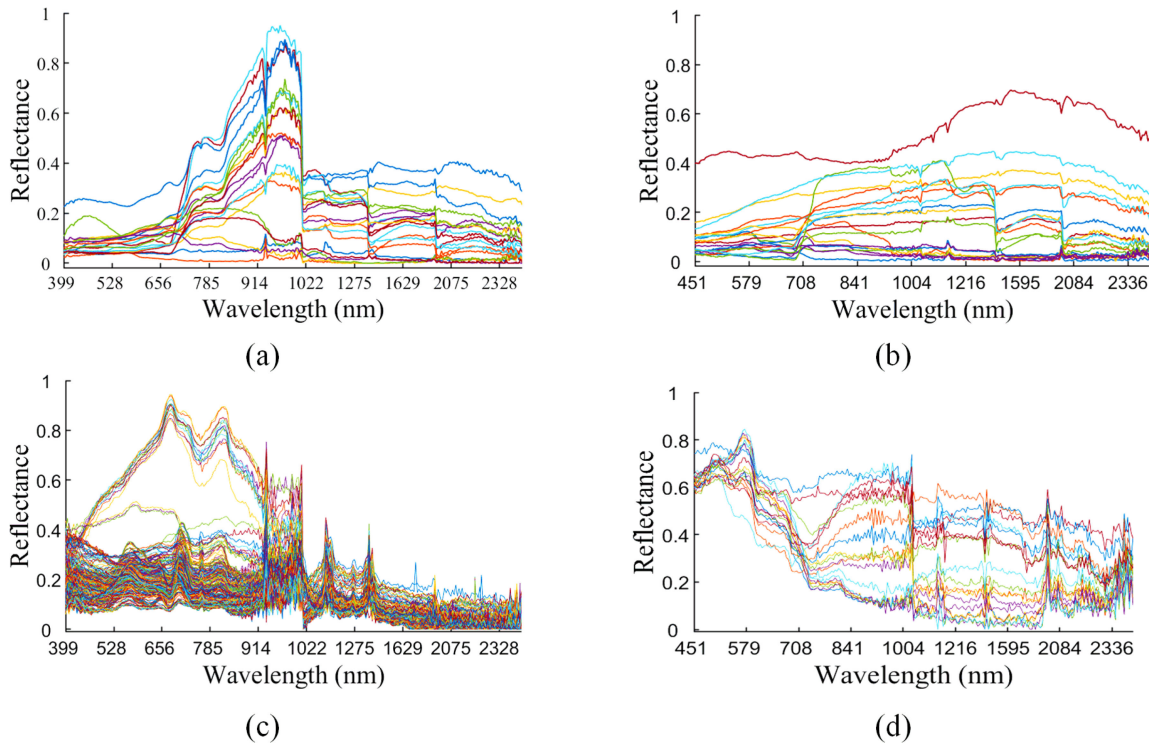

Fig. 2. Normalized spectrogram of GF-5 datasets. (a) and (b) display the spectrogram of each classes of Yellow River Estuary and Yancheng coastal wetland, (c) displays the spectrogram of the first class (*aquaculture*) of Yellow River Estuary samples, and (d) displays the spectrogram of the fifth class (*marsh*) of Yancheng coastal wetland samples. In order to study the spectral differences among different classes, we selected the mode of the sample spectrum of each class as the representative shown in (a) and (b). Single-class spectrograms are shown in (c) and (d) drawn from all samples spectra to study the intraclass spectral difference.

CNN-extracted features after HSI and MSI in regression domain are divided into blocks. Then, the high-level features are cascaded and fused. Compared with the simple data fusion method, this method can eliminate the redundant information caused by the correlation of multisource data in regression domain and obtain more discriminative information. Finally, the fused feature vectors are sent to a classifier that consists of fully connected layers with softmax loss to generate the fine classification results.

B. ICS_DLSR for Multisource Remote Sensing Data

First, visualization analysis is carried out for the necessity and effect of regression. After the spectral analysis of the two coastal wetlands datasets (to be introduced in Section IV-A), there are indeed small differences between classes and large differences within categories. The data normalized sample spectrograms of GF-5 data are shown in Fig. 2. It can be seen from the spectrogram of all categories [see Fig. 2(a) and (b)] that some
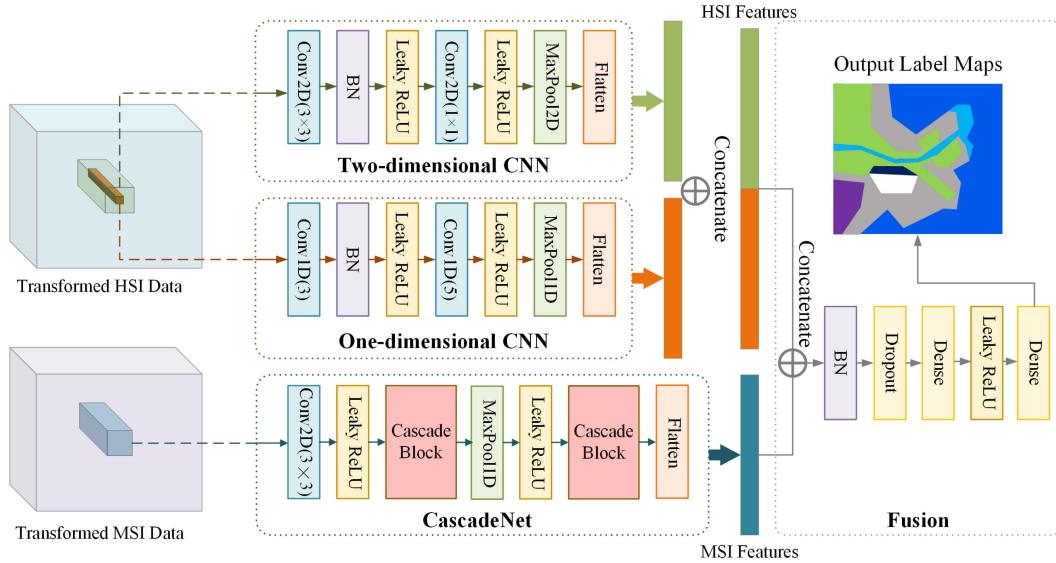
Fig. 3. Detailed structure of the regression domain feature extractor. The input data are a local patch around its center pixel. BN refers to batch normalization layer. Conv2D refers to the 2-D convolution layer.

spectral curves of different categories are highly coincident, and it is difficult to distinguish the network. For example, in Yellow River estuary wetland, the spectra of *Aquaculture*, *River*, *Shallow sea*, *Deep sea*, *Emergent vegetation*, and *Pond* are very similar. By carefully observing the Sentinel-2 image with high spatial resolution and Google Earth map details in the same location, it is found that aquaculture and emergent vegetation are highly mixed with sea area and water area, resulting in the phenomenon of same spectrum foreign matter in surface cover. However, *River*, *Shallow sea*, *Deep sea*, and *Pond* are all water sources, which are difficult to distinguish using HSI. Because of geographic information and hydrological conditions, they are divided into different categories. They can be distinguished with the assistance of spatial information. The same problems also exist in Yancheng coastal wetland data. In addition, there are obvious differences in the spectral curves of the same kind of samples in many categories, as shown in Fig. 2(c) and (d). Through the analysis of the samples block by block, it can be obtained that abnormal spectral samples appear mainly due to the block boundaries of aquaculture in the first type of *Aquaculture* samples of Yellow River Estuary data. For the fifth *Marsh* samples of Yancheng coastal wetland data, the differences of spectral features are mainly caused by different swamp vegetation coverage and different peat accumulation proportion.

It can be seen that the actual environment of coastal wetlands is extremely complex and dynamically changing, which bring great difficulty to classification. These problems are effectively solved after ICS_DLSR transformation. In the multisource remote sensing data of coastal wetlands, the labeling of the same location at the same time is invariant, and it is unconcerned with the spatial resolution of the sensor [49]. The training samples data matrix $X \in R^{m \times n}$, label matrix $Y \in R^{c \times n}$, and parameters λ_1, λ_2, and λ_3 are input into optimization problem (2); then, we initialized matrix $Q \in R^{c \times m}$ with random values: $F = QX, E = 0, C = 0, \mu = 10^{-8}, \mu_{\max} =$

10^8, and $\rho = 1.01$. Q, F, E, C, and μ are updated alternatingly until the minimum value of convergence is obtained and the transformation matrix Q is derived. Each training and testing sample is normalized to a unit vector. All samples are multiplied by Q to obtain the regression domain data.

C. Two-Branch CNN for Regression Domain Data

The detailed structure of regression domain feature extractor is shown in Fig. 3. Both spectral and spatial information are critical to HSI pixel-level classification. Therefore, the 2-D CNN classification framework is used to extract spectral–spatial features of the regressive HSI on the local patch. As shown in Fig. 3, the 2-D CNN consists of $r \times r \times L$ pixel blocks, and the 1-D CNN is composed of $1 \times 1 \times L$ pixel blocks (L is the number of bands). In 2-D CNN stream, each convolution process involves a certain operation, including 2-D CNNs (conv2D) and two batch normalization layers. All the convolution operations are executed with zero padding, and the convolution stride is set as 1. In addition, the activation function is Leaky ReLU, and Dropout is used to prevent overfitting [13]. In 1-D CNN stream, it is applied to extract spectral features, and on the contrary, convolution operations are executed without zero padding. Finally, both types of features are fused in the fully connected layer through concatenation.

The flowchart of CascadeNet stream to extract features in regressive MSI is also shown in Fig. 3. In this branch, the network is divided into three main parts: convolution layer, cascade block, and max-pool layer. In order to extract the spatial information around the sample and prevent redundancy, normalized data are first fed into the network following a convolutional operation with a spatial kernel (e.g., a 3×3 2-D kernel). Cascade block consists of seven layers of operations, including three convolution layers, two batch normalization, and leaky ReLU. There are two paths bridge, i.e., the first and middle convolution and

two activation operations. The path passes previous features to a subsequent layer with simple mathematical addition. Then, fused features are propagated to the next layer in the forward phase.

In the fusion stage, spatial features of HSI extracted by the 2-D CNN and spatial features of MSI extracted by CascadeNet are stacked. After batch normalization, the fused feature vector is classified by the fully connected layer.

D. Network Training Strategy

Usually, there are only a few training samples available for inner areas of coastal wetlands since they are scattered and difficult to access for labeling. But the external area is distributed in flakes, and samples are easy to collect. Thus, the sample equilibrium is very poor. In order to solve this problem, a randomly generated initialization seed is introduced in the training phase, which rotates at 90°, flipping left and right, and up and down. Therefore, additional samples can be added to the training set. All data are scaled to 0–1 to accelerate the convergence speed. Thanks to the technique of fine-tune's good performance, it is applied to transfer a pretrained model for large-scale data to small-scale and similar data [47].

In the training process of multisource data in regression domain, the two-branch network is trained with labeled samples separately; then, the high-level features of different domain for further merging are extracted by branches whose classifying layers are popped out. With an idea of transferred learning [65], the proposed network is further retrained to fine-tune the weights for better classification.

IV. EXPERIMENTAL RESULTS AND ANALYSIS

In this section, two coastal wetlands are selected for experimental study because of their abundant land cover types, which are Yellow River Estuary and Yancheng coastal wetland in China. The performance of the proposed method is compared with other state-of-the-art methods. For the proposed method, the regression transformation is implemented by MATLAB. Feature extraction and fusion classification are implemented in Python and Tensorflow with the high-level application programming interface Keras.

A. Study Area and Dataset Description

The Yellow River Delta is the fastest growing delta in the world, which is located in the northeast of Shandong Province, China (36°55'–38°16'N, 117°31'–119°18'E). As shown in Fig. 4(a), the Yellow River Estuary located in the east of Yellow River Delta has the total area of 2.424×10^3 km^2. The land covers of this study area are strongly influenced by salinization processes, and the vegetation mainly composes holophytic plant communities dominated by grass and shrub species [11], [12].

As shown in Fig. 4(b), Yancheng coastal wetland is located in the east of Jiangsu Province, China (32°34'–34°28'N, 119°27'–121°16'E), with the coastline length of 582 km and an area of 4.553×10^3 km^2. This area is rich in natural wetland resources,

with a large area of radiating sandbars, coastal forest farms and grasslands, and a wide coastal beach [66].

HSI data are captured by advanced hyperspectral imager, which is the main payload of the GF-5 satellite. MSI data are captured by the multispectral imager carried by Sentinel-2. Table I lists the information of satellite remote sensing data [17], [18], [67]. To keep the time consistency and reduce the negative effects from the changing land cover types in classification results, multisource remote sensing images are chosen with the acquisition time as close as possible. Some data preprocessing steps are essential before carrying out the proposed method, including spatial registration, geometric correction, atmospheric correction, image clipping, and merging. In addition, Sentinel-2 data need to be resampled and band splicing processing [12]. Then, based on GF-5 data, multisource optical remote sensing data are registered using the multiscale PIIFD descriptor [68]. Noisy and redundant bands are removed. The details of preprocessed images are listed in Table I. The pseudocolor images of HSIs and MSIs in two study areas are shown in Fig. 4(c)– (f).

The ground truth of the region of interest (ROI) is obtained using the field survey with global positioning system and with the help of high-spatial-resolution images. What is needed is that all spatial and spectral information has better not lost. Therefore, block scale transform is used for MSI before regression. In the subsequent padding period, the appropriate scale is selected for the two images to ensure the accuracy of classification. Training and testing samples are then randomly selected from the ROI, and their detailed information is listed in Table II. For sample collection, 21 land types from Yellow River Estuary and 20 land types from Yancheng coastal wetland are collected. To ensure a fair sampling condition, the number of training samples is almost three times that of testing samples. Since available sample labeling is obtained by field sampling in blocks, samples are distributed in small blocks with a small number. In order to simulate the real situation and realize the separation of training and testing samples, 10% blocks are randomly selected from each category as training and other blocks are used for testing. For convenience of observation, the ground truth maps of the two datasets and the selected training labels maps cover HSIs' pseudocolor images, as shown in Fig. 3(c) and (d). Table II lists the training and testing sample information and detailed category information of the data. For fair comparison, the number of training and testing samples of each data remains unchanged for all subsequent classifications.

B. Analysis on Regression Scheme

In order to evaluate the effectiveness of ICS_DLSR on classification, some popular LSR-based methods, including linear regression classification [69], sparse-representation-based classification [70], and kernel collaborative representation with Tikhonov regularization [71], are fairly evaluated on the Yellow river estuary and Yancheng coastal wetland datasets. K-nearest neighbor (KNN) is used to classify the results of feature transformation to compare performance. All methods are repeated ten times, and the average value of accuracies is reported in Table III. It is obvious that the ICS_DLSR obtains the best performance.
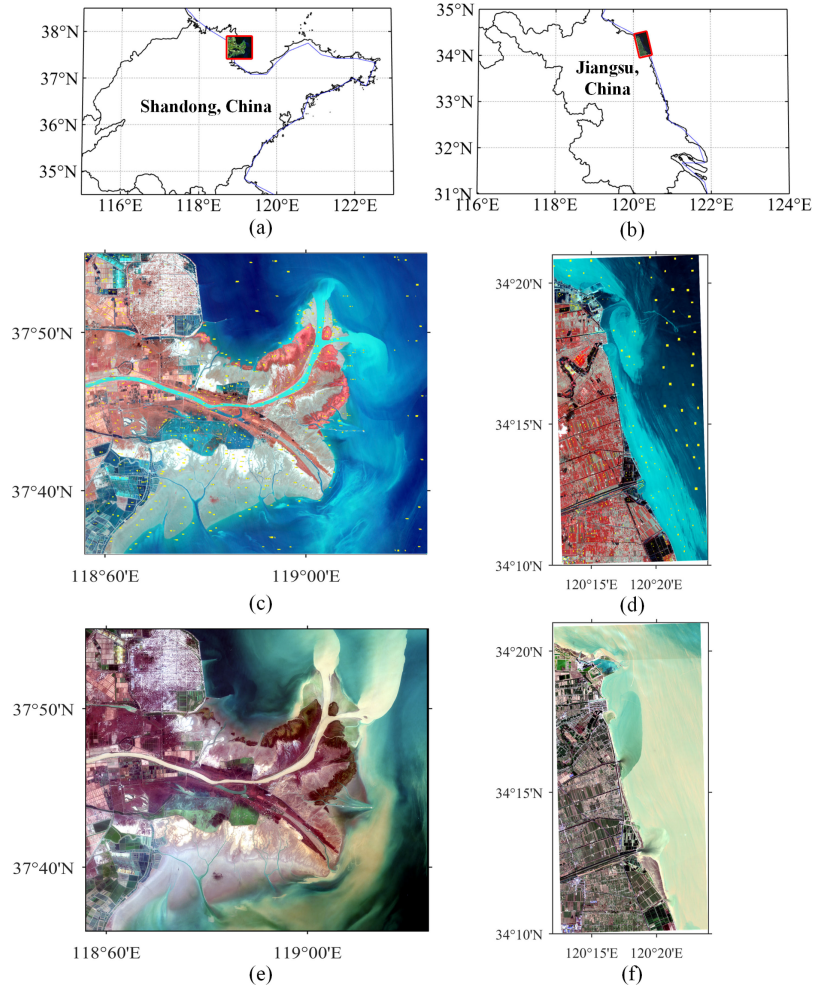
Fig. 4. Dataset visualization. (a) Location of Yellow River Estuary. (b) Location of Yancheng coastal wetland. (c) and (e) display pseudocolor images for HSI (R: Band140, G: Band40, and B: Band54) and MSI (R: Band2, G: Band3, and B: Band4) in Yellow River Estuary. (d) and (f) pseudocolor images for HSI (R: Band140, G: Band40, and B: Band54) and MSI (R: Band2, G: Band3, and B: Band4) in Yancheng coastal wetland. The yellow blocks in (c) and (d) refer to the location of the labeled samples.

TABLE I
LIST OF SATELLITE IMAGES DETAILS USED IN THIS STUDY

Study Areas	Satellites	Sensors	Track Number	Time	Spatial Resolution	Preprocessed size
Yellow River	GF-5	AHSI	002/571	2018/11/01	30m	1185×1342×285
Estuary Landsat	Sentinel-2	MSI	206/132	2018/11/03	10/20/60m	3555×4026×47
Yancheng coastal	GF-5	AHSI	002/571	2019/04/04	30m	1175×585×253
wetland Landsat	Sentinel-2	MSI	206/132	2019/03/29	10/20/60m	3525×1755×47

It can be seen that for the four datasets, the performance after ICS_DLSR consistently outperforms the original data, which proves the effectiveness of the regression. Among them, the improvement of GF-5 hyperspectral data is more obvious, which is due to abundant spectral information in HSIs. Regression processing based on sample correlation not only increases the margins of the samples, but also improves the problem of information redundancy.

Fig. 5 visualizes the margins of the samples before and after the transformation obtained by ICS_DLSR by using the t-SNE visualization. From this figure, the samples of the same class distribute closely and push samples of different classes far away as much as possible after data regression processing.

C. Parameter Tuning

1) Regression Parameter Tuning: In the ICS_DLSR transformation, there are three tuned parameters, i.e., λ_1, λ_2, and λ_3, which are used to balance the importance of the corresponding constraint terms. To learn the optimal transformation matrix for coastal wetlands datasets, while

TABLE II
DETAILS OF TRAINING AND TESTING SAMPLES FOR THE YELLOW RIVER ESTUARY AND YANCHENG COASTAL WETLAND DATASET

| No.	the Yellow River Estuary dataset Classes	Training ROI	Training Samples	Testing ROI	Testing Samples	No.	the Yancheng coastal wetland dataset Classes	Training ROI	Training Samples	Testing ROI	Testing Samples
1	Aquaculture	5	35	46	358	1	Sea	4	326	29	2069
2	Deep sea	3	87	23	709	2	Immediate offshore area	7	116	58	1189
3	Arable land	2	8	18	102	3	Salina	2	6	15	104
4	Phragmites	3	25	30	165	4	Pond	2	12	15	121
5	Rice field	3	11	29	72	5	Marsh	1	6	4	15
6	Sorghum	2	7	22	89	6	Spartina alterniflora loisel	2	7	15	76
7	Corn field	2	5	15	90	7	Mudflats	3	23	27	195
8	Soybean	5	18	42	193	8	Aquaculture	5	23	39	205
9	Low-tide mudflats	2	22	19	178	9	Paddy field	8	87	64	745
10	Shallow sea	5	89	41	847	10	Entrained water	3	24	25	148
11	Suaeda salsa	4	58	37	495	11	River	7	20	61	197
12	Yellow river	3	59	24	410	12	Woodland	2	16	18	140
13	Spartina alterniflora loisel	3	53	26	308	13	Barren	3	25	22	129
14	Freshwater herbaceous marshes	4	20	37	220	14	Buildings	5	21	41	339
15	High-tide mudflats	5	64	40	531	15	Fallow land	6	26	46	208
16	Intertidal saltwater marshes	3	53	25	401	16	Dry land	4	28	33	176
17	Intertidal phragmites	3	17	23	116	17	Suaeda	2	43	14	42
18	Fishponds	3	51	25	326	18	Mariculture	2	6	19	29
19	Tamarix	2	6	15	62	19	Irrigation canal	2	5	17	33
20	Locust	2	7	14	65	20	Phragmites	3	12	20	120
21	Emergent vegetation	1	9	8	30						
	Total	65	704	559	5767		Total	73	832	582	6280

(a) (b) (c) (d)
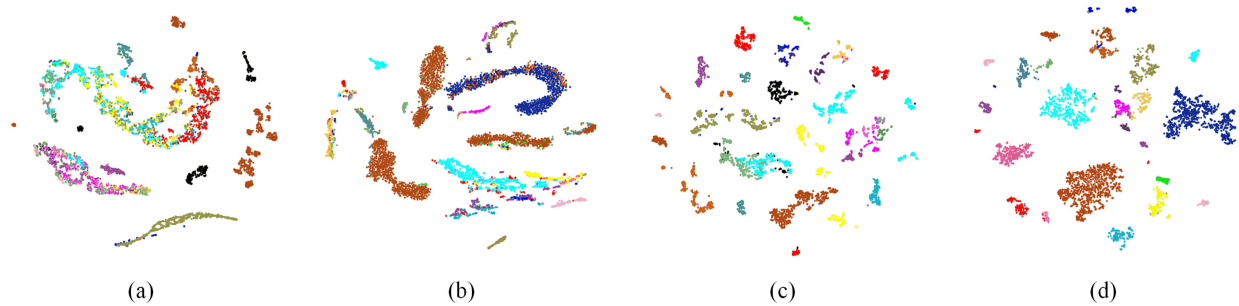
Fig. 5. T-SNE visualization of (a) and (b) the original features of Yellow River Estuary and Yancheng coastal wetland and (c) and (d) the transformed features of Yellow River Estuary and Yancheng coastal wetland obtained by ICS_DLSR on the GF-5 data. Training samples in Table II are used to learn the transformation. All samples, including training and testing samples, are visualized.

TABLE III
CONTRAST EXPERIMENT OF DIFFERENT LSR WITH THE KNN CLASSIFIER
USING FOUR IMAGES

Methods	Yellow River Estuary GF-5	Yellow River Estuary Sentinel-2	Yancheng coastal wetland GF-5	Yancheng coastal wetland Sentinel-2
Original	78.03%	68.89%	81.10%	63.29%
LRC	83.37%	73.54%	88.12%	68.79%
SRC	88.54%	76.48%	89.45%	71.29%
CRT	91.37%	81.25%	92.56%	70.23%
ICS_DLSR	91.75%	80.89%	93.15%	72.77%

referring to the parameter settings in the candidate set $\{1e^{-3}, 5e^{-3}, 1e^{-2}, 5e^{-2}, 1e^{-1}, 5e^{-1}, 1, 5, 10\}$, we then performed ICS_DLSR with different combinations of these parameters. Fig. 6(a) shows the relationships of the three parameters

and the classification accuracy on Yellow River Estuary datasets. Finally, $\lambda_1 = 10$, $\lambda_2 = 0.5$, and $\lambda_3 = 0.1$ are selected. Under this parameter combination, the objective function value drops the fastest. Since the two wetland datasets were shot by the same satellite, respectively, with the same resolution and similar sample size, the characteristics of the two wetland datasets obtained from the spectral analysis in Fig. 2 and T-SNE visualization in Fig. 5. are similar, so the two datasets use the same regression parameters.

2) CNN Parameter Tuning: The network of the branch has complex architecture with more parameters. Therefore, it is time consuming to train this network until its convergence. The main network architecture of the two-branch CNN is shown in Table IV. The size of convolution kernel and the dimension of feature map are set. Besides, the effect of several different sizes of the pixel block is investigated in the original domain feature extractor, since the surrounding pixels are critical to the central
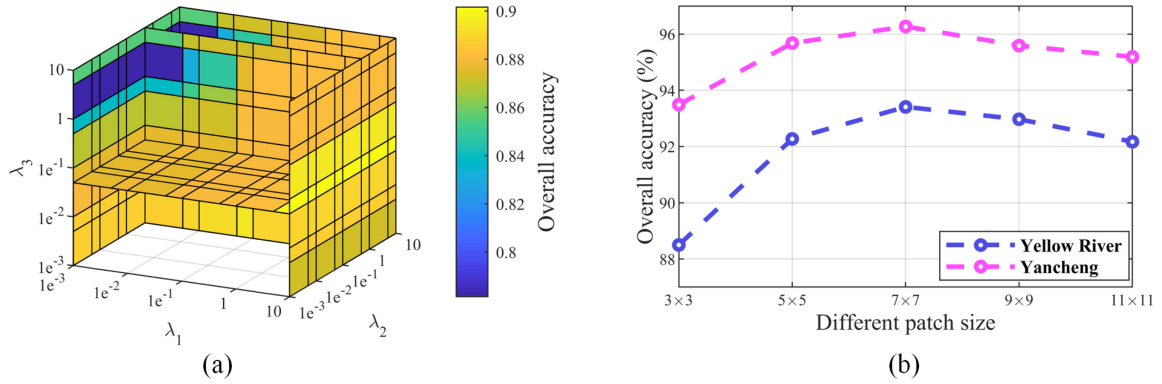
Fig. 6. Value of OA in Yellow River Estuary when the parameter changes. (a) Effect of three regression parameters on OA with the classification method in [55]. For the convenience of clear presentation, slice at $\lambda_1 = 1e^{-3}, 10$, $\lambda_2 = 5e^{-2}, 10$, and $\lambda_3 = 5e^{-2}$. Different colors are used to represent OA values, and the corresponding relationship between color and OA is shown colormap. (b) Effect of the local input patch size on OA with the proposed method.

TABLE IV
DETAILS OF THE MULTISTREAM CNN ARCHITECTURE

HSI 2-D Tunnel			MSI Tunnel		
Layer	Kernel Size	Activation	Layer	Kernel Size	Activation
input (15×15×B1)			input (15×15×B2)		
Conv2D_1	3×3×256	LeakyReLU	Conv2D_1	3×3×64	LeakyReLU
Conv2D_2	1×1×512	LeakyReLU	Conv2D_2	3×3×128	
MaxPool2D	2×2		Conv2D_3	1×1×64	LeakyReLU
Flatten (32768)			Conv2D_4	3×3×128	
HSI 1-D Tunnel			Add (Conv2D_2, Conv2D_4)		
Layer	Kernel Size	Activation	Conv2D_5	1×1×64	LeakyReLU
input (1×1×B1)			Add (Conv2D_3, Conv2D_5)		
Conv1D_1	11×64	LeakyReLU	Conv2D_6	1×1×64	LeakyReLU
Conv1D_2	3×128	LeakyReLU	MaxPool2D	2×2	LeakyReLU
MaxPool1D	2×1		Conv2D_7	3×3×256	
Flatten (512)			Conv2D_8	1×1×128	LeakyReLU
			Conv2D_9	3×3×256	
			Add (Conv2D_7, Conv2D_9)		
			Conv2D_10	1×1×128	LeakyReLU
			Add (Conv2D_8, Conv2D_10)		
			Conv2D_11	1×1×128	LeakyReLU
Fully Connected-33280			Flatten (8192)		
Fully Connected-41472					
Fully Connected-128					
Soft-max					

B1 and B2 refer to the bands of HSI and MSI.

pixel. Several different window sizes of {$3 \times 3, 5 \times 5, 7 \times 7, 9 \times 9, 11 \times 11$} are tested. The overall accuracy (OA) result is shown in Fig. 6(b). After measuring the OA results and the amount of network calculation, the input radius is selected as 7×7. The number of training epochs and batch size are empirically set to 30 and 100, respectively. Besides, the learning rate is one of the factors that affects the convergence of speed and training performance. The learning rate is set as 0.01 with the policy of Adam [47].

D. Classfication Performance

To illustrate the performance of the proposed method for coastal wetland data classification, it is compared with several classical classifiers, such as SVM [72], LBP-ELM [73], and the recently developed CNN-type methods, such as CD-CNN [35], dual-tunnel CNN [47], and CascadeNet [63]. In order to verify the validity of data fusion on coastal wetlands datasets, each method tests in three cases. They are HSI data only, MSI data only, and HSI and MSI combined data. The combined data strategy here is the commonly used pixel-level image composite method. The SVM is implemented using the LIBSVM toolbox. All of the experiments are repeated ten times, and the average results with standard variations are reported. Tables V and VI list the class-specific accuracy, OA, average accuracy (AA), and Kappa statistic of these methods for two datasets.

Judging from the classification results of different data sources of each method, the accuracy of classification by fused data is always better than that of single-source data classification, which proves that the feature fusion strategy effectively combines the advantages of both data sources in coastal wetlands mapping task.

From the results of each individual experimental data, the proposed method yields the best OA, AA, and Kappa with a significant improvement over the reference methods for the two coastal wetlands datasets. According to the experimental analysis using the same fused dataset, the proposed method achieves the gains of about 4% over the SVM method with high dependence on clear samples margins. Compared with LBP-ELM based on data change fitting and texture relationship extraction, it has increased by about 1.7–3.8%. Due to the small amount of coastal wetland data, classification results of three CNN-type methods are not so good, and the accuracy from the proposed method is about 4–5% higher than other CNN algorithms, which effectively proves that it has stronger robustness in the case of small samples. Meanwhile, the proposed method effectively improves the classification of categories that are difficult to distinguish by other methods (e.g., the fifth class of Yancheng wetland data). The AA and Kappa parameters of the proposed

TABLE V
COMPARISON OF THE CLASSIFICATION ACCURACY (%) AMONG THE PROPOSED METHOD AND THE OTHERS USING YELLOW RIVER ESTUARY DATASET

No.	SVM			LBP-ELM			CD-CNN			Dual-tunnel CNN			CascadeNet			Multi-stream CNN
	GF5	Sen2	GF5+Sen	GF5	Sen2	GF5+Sen	GF5	Sen2	GF5+Sen	GF5	Sen2	GF5+Sen	GF5	Sen2	GF5+Sen	
1	64.69	73.96	89.55	94.13	49.72	94.69	95.31	71.32	85.89	90.97	82.35	89.29	71.18	73.29	86.60	86.39±1.09
2	**100.00**	86.79	99.02	75.18	65.87	98.87	96.87	83.69	99.85	95.30	77.30	**100.00**	98.02	89.35	**100.00**	**100.00±0.00**
3	74.75	81.37	88.89	96.08	91.18	85.29	69.18	50.30	75.37	72.79	71.05	68.92	76.12	65.32	62.96	73.88±7.46
4	83.63	79.92	84.80	86.67	81.82	86.67	86.67	79.41	95.33	97.54	78.17	**100.00**	99.25	76.19	95.33	97.28±6.8
5	14.00	38.34	8.00	54.17	11.11	22.22	77.27	95.65	**100.00**	100.00	100.00	94.29	95.65	**96.30**	**100.00**	**100.00±0.00**
6	26.44	50.51	87.36	98.88	55.06	88.76	84.85	97.14	**100.00**	100.00	100.00	**100.00**	97.14	87.50	**100.00**	96.10±5.19
7	55.81	85.84	77.91	**100.00**	91.11	97.78	84.11	75.00	98.63	97.78	92.47	98.90	75.00	70.69	86.54	97.83±2.17
8	**100.00**	93.45	98.95	**100.00**	98.96	**100.00**	97.11	77.11	96.50	97.97	79.01	**100.00**	92.34	81.01	85.78	92.68±4.88
9	56.11	**100.00**	93.89	99.44	**100.00**	99.44	97.27	76.39	**100.00**	98.88	65.93	96.77	94.68	70.94	97.65	99.44±2.77
10	92.41	71.83	90.63	87.72	49.47	77.45	61.97	54.19	86.57	83.85	51.79	66.48	85.74	55.82	72.57	**92.54±0.04**
11	98.19	98.15	98.80	99.80	98.38	99.80	96.46	89.68	94.06	97.44	85.71	99.40	95.56	89.03	98.59	96.30±1.94
12	**100.00**	**100.00**	**100.00**	**100.00**	**100.00**	**100.00**	97.62	88.17	99.51	**100.00**	89.13	99.76	89.17	95.35	**100.00**	**100.00±0.00**
13	99.38	98.46	98.15	99.03	99.03	99.35	**100.00**	95.36	94.87	99.33	91.94	**100.00**	95.56	87.25	95.22	91.67±2.38
14	77.31	77.62	71.30	84.09	90.91	90.00	83.76	79.82	67.97	66.24	84.92	89.73	71.43	83.92	80.58	87.36±4.94
15	**100.00**	96.02	**100.00**	**100.00**	95.10	**100.00**	99.62	95.78	99.07	99.81	95.32	94.52	98.15	**96.36**	98.88	95.40±1.85
16	99.51	64.87	98.29	99.25	85.79	**100.00**	99.50	77.15	98.04	99.75	81.93	**100.00**	92.77	79.39	97.05	**100.00±0.00**
17	83.33	75.23	78.33	89.66	91.38	93.10	87.30	66.01	85.16	85.22	63.57	92.24	81.20	56.41	72.97	**94.34±4.72**
18	80.59	40.60	64.71	75.15	83.44	81.60	52.38	52.31	49.90	46.69	32.95	55.61	39.51	47.54	49.81	**88.06±3.22**
19	75.81	84.75	81.61	80.65	66.13	12.90	75.00	65.63	62.50	11.11	81.25	64.79	53.57	63.10	69.05	76.32±13.16
20	75.38	71.06	52.31	92.31	52.31	86.15	98.39	**100.00**	98.33	92.31	83.33	98.46	89.55	71.62	91.94	**100.00±0.00**
21	97.22	91.46	97.22	93.33	90.00	96.67	**100.00**	52.63	93.33	61.36	50.00	86.21	74.36	41.10	64.86	**100.00±0.00**
OA (%)	87.19	81.46	89.85	91.05	78.57	91.66	85.45	76.54	88.54	87.86	74.51	88.54	85.33	77.20	86.02	**93.41±0.46**
AA (%)	78.79	79.06	83.80	90.74	78.42	86.23	87.40	77.27	89.57	85.44	78.01	90.26	84.09	75.12	86.02	**93.60±3.03**
Kappa	0.8744	0.8012	0.8898	0.9029	0.7691	0.9096	0.8426	0.7729	0.8769	0.8687	0.7549	0.8758	0.8417	**0.7541**	0.8488	**0.9286±0.0053**

TABLE VI
COMPARISON OF THE CLASSIFICATION ACCURACY (%) AMONG THE PROPOSED METHOD AND THE OTHERS USING YANCHENG COASTAL WETLAND DATASET

No.	SVM			LBP-ELM			CD-CNN			Dual-tunnel CNN			CascadeNet			Multi-stream CNN
	GF5	Sen2	GF5+Sen	GF5	Sen2	GF5+Sen	GF5	Sen2	GF5+Sen	GF5	Sen2	GF5+Sen	GF5	Sen2	GF5+Sen	
1	95.63	93.56	92.76	92.51	71.92	92.51	99.41	83.43	99.13	99.38	73.42	**100.00**	99.49	78.51	**100.00**	**100.00±0.00**
2	94.13	32.90	**100.00**	98.77	70.56	**100.00**	99.75	52.93	99.26	99.75	53.27	99.92	99.66	69.51	**100.00**	**100.00±0.00**
3	71.72	68.57	29.29	62.50	10.58	29.81	80.00	88.41	77.78	41.27	78.95	29.67	83.33	92.86	36.72	80.25±20.51
4	87.50	83.67	**100.00**	84.30	66.12	84.30	81.13	100.00	100.00	**100.00**	95.00	97.75	**100.00**	100.00	100.00	**100.00±0.00**
5	21.05	5.26	0.00	60.00	66.67	40.00	1.96	76.67	11.03	13.33	66.67	65.30	4.81	25.00	11.90	88.24±16.02
6	**100.00**	95.84	**100.00**	**100.00**	64.47	**100.00**	94.52	37.93	91.46	97.87	45.45	**100.00**	96.30	79.25	98.51	96.15±0.15
7	88.83	86.92	93.91	90.77	92.82	92.82	60.43	64.21	57.47	97.42	45.40	93.99	84.91	72.33	85.32	**96.76±0.54**
8	96.06	73.74	93.20	89.76	70.24	95.12	93.46	89.81	91.90	89.73	90.63	97.99	83.61	67.38	97.03	**98.55±0.97**
9	99.20	85.28	99.20	98.52	82.68	99.73	93.27	89.21	98.41	88.57	86.00	97.13	94.49	91.39	98.02	99.46±0.41
10	90.97	35.44	97.42	91.22	37.84	92.57	58.54	40.49	70.71	89.16	55.64	59.50	84.00	44.34	93.67	86.05±5.81
11	95.92	52.96	63.78	98.48	71.57	93.91	69.58	82.20	83.49	79.82	77.83	74.13	82.01	79.34	81.67	89.50±0.91
12	21.99	79.51	97.16	98.57	17.86	94.29	71.43	95.12	86.96	92.78	**100.00**	97.90	97.22	**100.00**	97.90	**100.00±0.00**
13	92.81	67.07	97.84	**100.00**	93.02	**100.00**	55.19	85.11	84.78	93.98	88.72	51.39	43.86	97.54	76.10	86.58±6.71
14	91.98	78.22	72.53	47.49	60.18	85.25	95.33	97.86	**100.00**	100.00	96.89	98.60	94.14	97.12	82.48	**100.00±0.00**
15	80.57	68.67	99.05	99.52	41.35	75.96	82.61	65.58	88.61	79.15	60.77	87.84	96.84	48.72	**100.00**	91.28±4.52
16	11.09	32.97	98.91	91.48	65.91	97.73	81.16	44.00	78.22	65.57	38.69	92.74	68.97	54.17	87.10	95.00±0.56
17	97.40	0.00	76.62	88.10	54.76	80.95	47.41	48.78	56.16	71.43	41.98	46.34	58.82	26.53	38.10	80.77±3.85
18	62.50	57.04	0.00	**100.00**	55.17	51.72	65.52	81.82	**100.00**	76.32	71.79	80.65	70.27	81.82	48.28	72.50±12.5
19	14.29	23.70	5.71	69.70	60.61	87.88	**100.00**	100.00	50.00	93.75	**100.00**	**100.00**	73.68	84.62	50.00	91.67±8.33
20	98.32	71.78	97.48	63.33	51.67	75.00	95.65	83.53	**100.00**	90.82	94.52	**100.00**	98.57	87.34	**100.00**	99.14±0.86
OA (%)	90.97	70.88	91.61	91.27	68.26	92.47	88.05	71.91	92.06	91.49	69.39	92.60	90.64	76.10	92.50	**96.27±0.15**
AA (%)	75.60	59.66	75.74	86.25	60.30	83.48	76.32	75.35	81.27	83.01	73.08	85.28	80.75	73.89	79.14	**91.09±1.28**
Kappa	0.9007	0.6454	0.8997	0.8960	0.6198	0.9102	0.8574	0.6674	0.9033	0.8976	0.6835	0.9113	0.8880	0.7112	0.9104	**0.9552±0.0019**

TABLE VII
ABLATION ANALYSIS EXPERIMENT IN TWO DATASETS

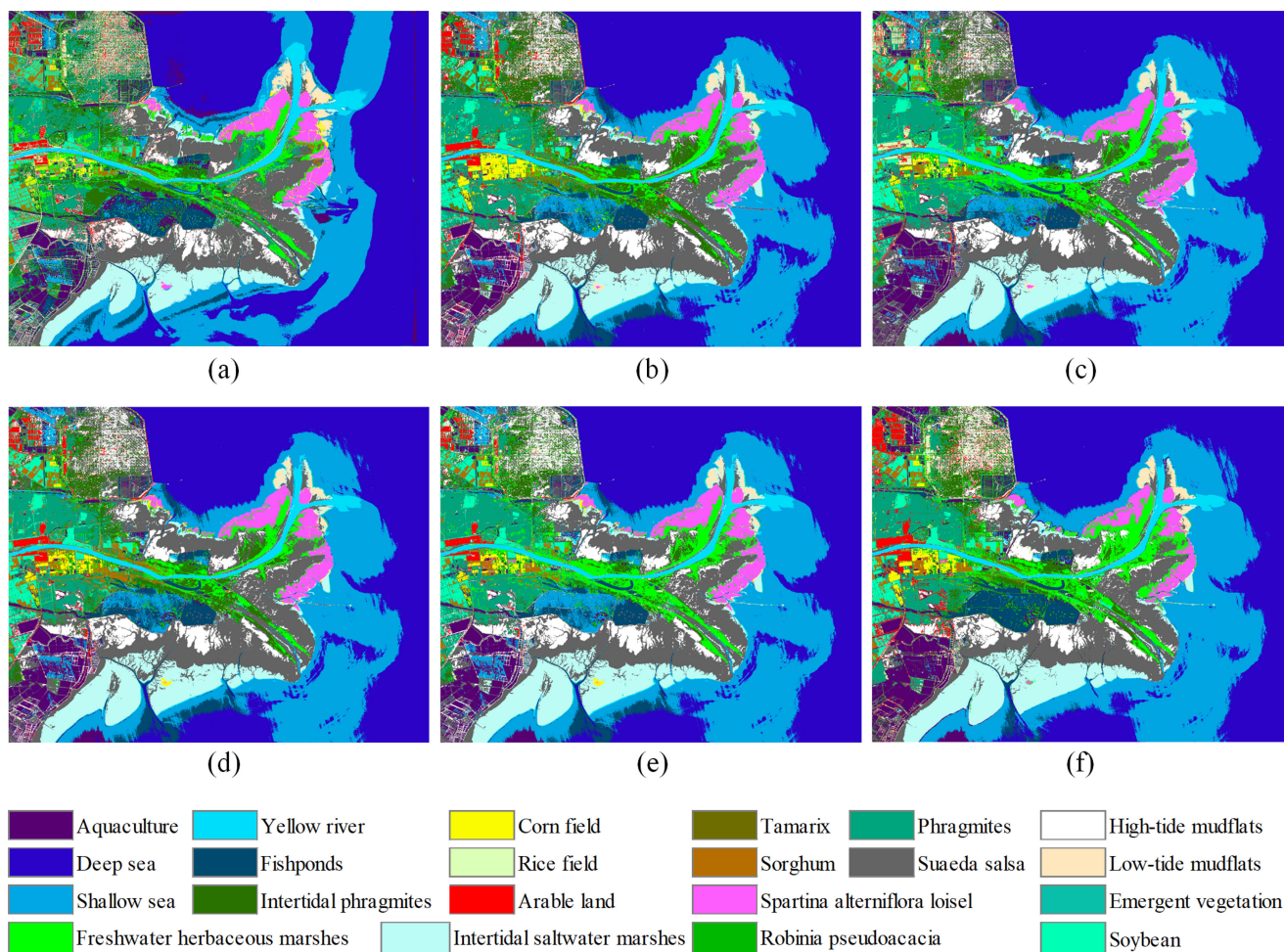|	Yellow River Estuary				Yancheng coastal wetland			
Regression	✗	✓	✓	✓	✗	✓	✓	✓
Cascade Net	✓	✓	✗	✓	✓	✓	✗	✓
Dual-tunnel CNN	✓	✗	✓	✓	✓	✗	✓	✓
OA(%)	89.50	86.06	93.38	93.41	92.96	82.55	94.16	96.27
Kappa	0.8840	0.8436	0.9282	0.9286	0.9324	0.8487	0.9303	0.9552

Fig. 7. Full classification maps on the Yellow River Estuary multisource dataset obtained by (a) SVM, (b) LBP-ELM, (c) CD-CNN, (d) dual-tunnel CNN, (e) CascadeNet, and (f) the proposed multistream CNN.

method are the highest, demonstrating that the proposed method achieves the best performance in class equilibrium.

Based on the experimental results using single-source datasets, it can be seen that in the CNN-type methods, spectral and spatial features can be extracted simultaneously, such as CD-CNN and dual-tunnel CNN methods, which has a good classification effect on HSI. Among them, the dual-tunnel CNN method of feature fusion after extracting spectral and spatial information separately has higher mapping accuracy. Compared with the CD-CNN method that uses multiscale convolutional filter bank extract local block information, the CascadeNet methods extracting multiple scales information have a better classification effect on MSIs. Compared with the CD-CNN method that explores local contextual interactions, CascadeNet, which integrates features of different layers and scales, has higher classification accuracy for coastal wetland MSI. It further proves the reliability of the proposed method fusing the MSI features extracted from CascadeNet methods and the HSI features extracted by the dual-tunnel CNN.

The experimental results of the ICS_DLSR regression, CascadeNet, and dual-tunnel CNN are shown in Table VII for a further quantitative ablation analysis, where $\sqrt{}$ means that part

is employed and $\times$ means that part is not employed. Classification results are obtained by the partial combinations shown in each column. The CascadeNet stream and the dual-tunnel CNN stream were used separately in the corresponding single source data. The results of the single branch in the fused data are shown in Tables V and VI. It can be seen that in two datasets that the classification accuracy of our method in columns 5 and 9 is the highest of the list. The ablation experiments prove that these three parts are all necessary for this classification.

Using the fused data and 10% of the labeled samples as the training set, all samples in the dataset are classified and mapped. As in Figs. 7 and 8, the full classification maps obtained by the proposed method contain more detailed information, and the boundary of the feature type area is also clearer. Furthermore, the proposed method presents more similar results to the reference map in Fig. 3. Exhibiting smoother appearance than other reference methods proves more robust spectral and spatial features.

To verify the generalization ability of the proposed method on different numbers of training samples, 10%, 30%, 50%, and 90% samples block per class are randomly chosen as training data for two datasets, and the fused data are used for
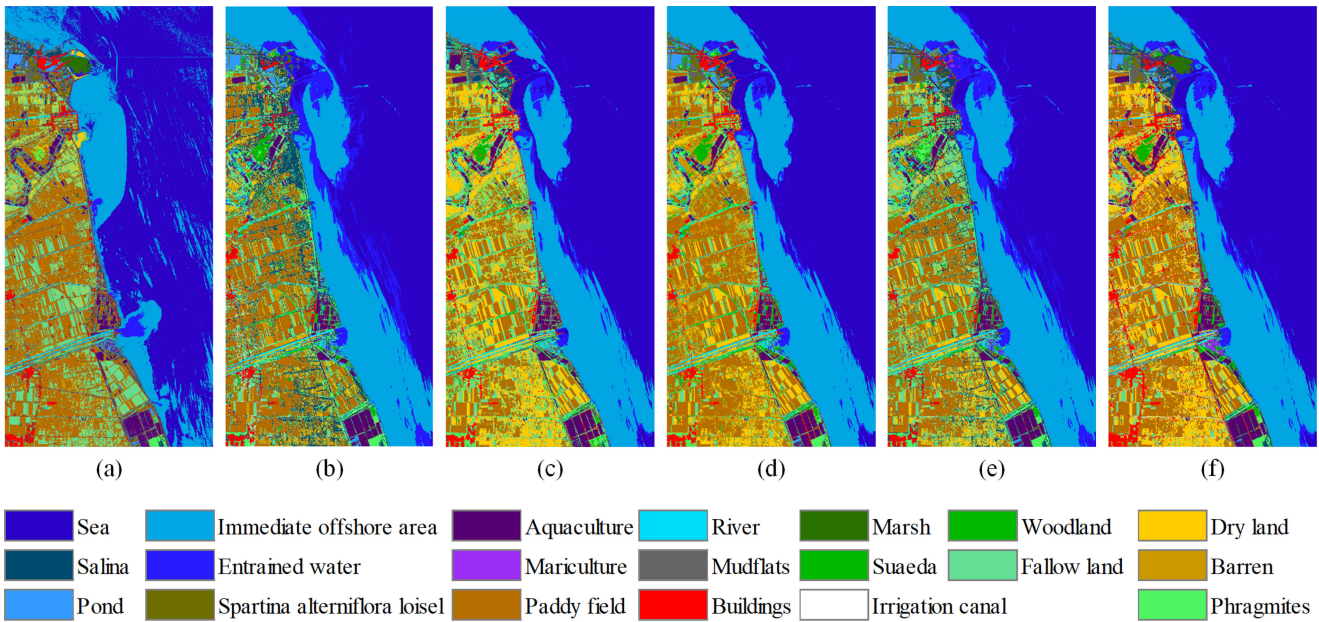
Fig. 8. Full classification maps on the Yancheng coastal wetland multisource dataset obtained by (a) SVM, (b) LBP-ELM, (c) CD-CNN, (d) dual-tunnel CNN, (e) CascadeNet, and (f) the proposed multistream CNN.
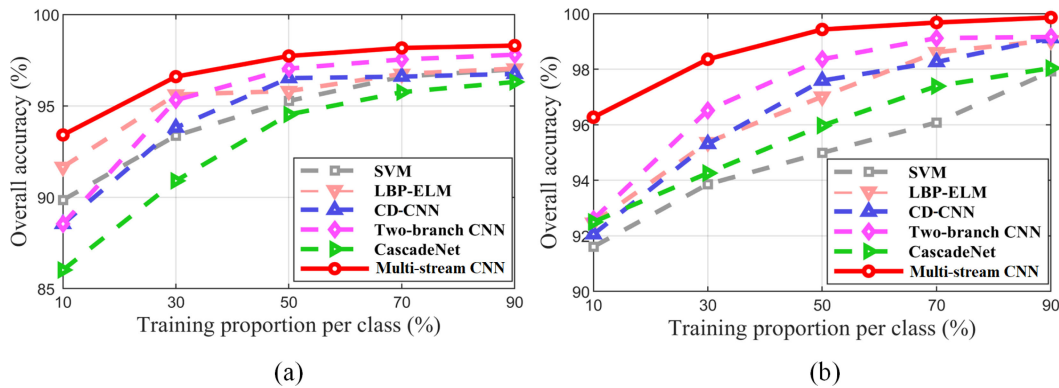

Fig. 9. OA of different methods with different numbers of training samples per class. (a) Yellow River Estuary multisource dataset. (b) Yancheng coastal wetland multisource dataset.

classification. Fig. 9 shows the OA for the proposed method and five kinds of reference methods. Clearly, all the methods yield better classification performance as the number of training samples increases. The proposed method consistently provides superior OA compared with the reference methods for two datasets. Especially, when the number of the labeled training data is limited, the proposed method has an obvious advantage in terms of classification performance over the reference methods. It proves that the proposed method exhibits robust classification performance for balanced and unbalanced training samples.

V. CONCLUSION

In this article, an effective multistream CNN method is proposed to improve feature extraction capability for coastal wetland mapping, where the CNN architecture is designed to combine features extracted from multisource remote sensing data after regression processing. With the proposed method,

each class of samples was transformed to a more discriminative space, and high-resolution spatial information and spectral information are effectively combined, leading to the improvement of the overall classification accuracy. Experimental results have demonstrated the effectiveness of the proposed method for more than 20 object types in the Yellow River Estuary dataset and the Yancheng coastal wetland dataset captured by GF-5 and Sentinel-2 satellites, and the statistical performance of this method is better than state-of-the-art classifiers when the training sample size is small.

REFERENCES

[1] S. Hu, Z. Niu, and Y. Chen, "Global wetland datasets: A review," *Wetlands*, vol. 37, no. 5, pp. 1943–6246, Oct. 2017.

[2] E. Adam, O. Mutanga, and D. Rugege, "Multispectral and hyperspectral remote sensing for identification and mapping of wetland vegetation: A review," *Wetlands Ecol. Manage.*, vol. 18, no. 3, pp. 281–296, Dec. 2010.

[3] G. Meng, L. Jing, S. Chunlei, X. Jiawei, and W. Li, "A review of wetland remote sensing," *Sensors*, vol. 17, no. 4, 2017, Art. no. 777.

[4] T. Spencer *et al.*, "Global coastal wetland change under sea-level rise and related stresses: The DIVA wetland change model," *Global Planet. Change*, vol. 139, pp. 15–30, Apr. 2016.

[5] M. Schuerch *et al.*, "Future response of global coastal wetlands to sea-level rise," *Nature*, vol. 561, no. 231, pp. 1476–4687, 2018.

[6] H. Akira, M. Marguerite, and W. Roy, "Hyperspectral image data for mapping wetland vegetation," *Wetlands*, vol. 23, no. 2, pp. 436–448, Jun. 2003.

[7] X. Wang, X. Gao, Y. Zhang, X. Fei, and H. Zhao, "Land-cover classification of coastal wetlands using the RF algorithm for WorldView-2 and Landsat 8 images," *Remote Sens.*, vol. 11, no. 16, Aug. 2019, Art. no. 1927.

[8] R. J. Zomer, A. Trabucco, and S. L. Ustin, "Building spectral libraries for wetlands land cover classification and hyperspectral remote sensing," *J. Environ. Manage.*, vol. 90, no. 7, pp. 2170–2177, Oct. 2009.

[9] B. Lehner and P. Doll, "Development and validation of a global database of lakes, reservoirs and wetlands," *J. Hydrol. Amsterdam*, vol. 296, no. 4, pp. 1–22, 2004.

[10] Y. Hu, J. Zhang, Y. Ma, J. An, G. Ren, and X. Li, "Hyperspectral coastal wetland classification based on a multiobject convolutional neural network model and decision fusion," *IEEE Geosci. Remote Sens. Lett.*, vol. 16, no. 7, pp. 1110–1114, Jul. 2019.

[11] H. Yabin, Z. Jie, M. Yi, L. Xiaomin, S. Qinpei, and J. An, "Deep learning classification of coastal wetland hyperspectral image combined spectra and texture features: A case study of Huanghe (Yellow) River Estuary wetland," *Acta Oceanologica Sinica*, vol. 38, no. 5 pp. 142–150, May 2019.

[12] L. Jiao, W. Sun, G. Yang, G. Ren, and Y. Liu, "A hierarchical classification framework of satellite multispectral/hyperspectral images for mapping coastal wetlands," *Remote Sens.*, vol. 11, no. 19, pp. 2238–2259, Dec. 2019.

[13] L. Gao, D. Hong, J. Yao, B. Zhang, G. Paolo, and C. Jocelyn, "Spectral superresolution of multispectral imagery with joint sparse and low-rank learning," *IEEE Trans. Geosci. Remote Sens.*, to be published.

[14] W. Sun and Q. Du, "Graph-regularized fast and robust principal component analysis for hyperspectral band selection," *IEEE Trans. Geosci. Remote Sens.*, vol. 56, no. 6, pp. 3185–3195, Jan. 2018.

[15] Y. Samantha, L. Virginie, A. Didier, C. Cecile, D. Aurelie, and B. Marie-Lise, "Classification and mapping of saltmarsh vegetation combining multispectral images with field data," *Estuarine, Coastal, Shelf Sci.*, vol. 236, 2020, Art. no. 106643.

[16] S. Andrey, M. Maria, M. Alexander, and V. Anna, "Assessing the land and vegetation cover of abandoned fire hazardous and rewetted peatlands: Comparing different multispectral satellite data," *Land*, vol. 7, no. 2, Dec. 2018, Art. no. 71.

[17] S. Renato and M. Domenica, "Lago grande in Monticchio area (Southern Italy): Integrating multitemporal airborne images, satellite images (Sentinel-2)," *Int. J. Agriculture Sustain. Develop.*, vol. 2, no. 1, pp. 1–23, Mar. 2020.

[18] A. Zhang, G. Sun, P. Ma, X. Jia, and X. Zhang, "Coastal wetland mapping with Sentinel-2 MSI imagery based on gravitational optimized multilayer perceptron and morphological attribute profiles," *Remote Sens.*, vol. 11, no. 8, pp. 952–975, Apr. 2019.

[19] W. Jingzheng *et al.*, "Machine learning-based detection of soil salinity in an arid desert region, Northwest China: A comparison between Landsat-8 OLI and Sentinel-2 MSI," *Sci. Total Environ.*, vol. 707, no. 10, Mar. 2020, Art. no. 136092.

[20] X. Han, J. Pan, and A. T. Devlin, "Remote sensing study of wetlands in the Pearl river delta during 1995–2015 with the support vector machine method," *Front. Earth Sci.*, vol. 12, no. 3, pp. 521–531, Mar. 2018.

[21] J. Liu, Q. Feng, J. Gong, J. Zhou, and Y. Li, "Land-cover classification of the Yellow river delta wetland based on multiple end-member spectral mixture analysis and a random forest classifier," *Int. J. Remote Sens.*, vol. 37, no. 8, pp. 1845–1867, Apr. 2016.

[22] J. Reschke and C. üttich, "Continuous field mapping of mediterranean wetlands using sub-pixel spectral signatures and multi-temporal landsat data," *Int. J. Appl. Earth Observ. Geoinf.*, vol. 28, pp. 220–229, 2014.

[23] D. Pierre, K. Douglas, U. Dikaso, and R. Lisa-Maria, "Mapping the Dabus Wetlands, Ethiopia, using random forest classification of landsat, PALSAR and topographic data," *Remote Sens.*, vol. 9, no. 10, pp. 1056–1079, Oct. 2017.

[24] M. J. Mccarth *et al.*, "Satellite remote sensing for coastal management: A review of successful applications," *Environ. Manage.*, vol. 60, no. 2, pp. 323–339, Jan. 2017.

[25] A. J. Rebelo, B. Somers, K. J. Esler, and P. Meire, "Can wetland plant functional groups be spectrally discriminated?," *Remote Sens. Environ.*, vol. 210, pp. 25–34, 2018.

[26] X. Kang, S. Li, L. Fang, M. Li, and J. A. Benediktsson, "Extended random walker-based classification of hyperspectral images," *IEEE Trans. Geosci. Remote Sens.*, vol. 53, no. 1, pp. 144–153, Jan. 2015.

[27] X. Kang, S. Li, L. Fang, and J. A. Benediktsson, "Intrinsic image decomposition for feature extraction of hyperspectral images," *IEEE Trans. Geosci. Remote Sens.*, vol. 53, no. 4, pp. 2241–2253, Apr. 2015.

[28] P. Duan, X. Kang, S. Li, P. Ghamisi, and J. A. Benediktsson,"Fusion of multiple edge-preserving operations for hyperspectral image classification," *IEEE Trans. Geosci. Remote Sens.*, vol. 57, no. 12, pp. 10336–10349, Dec. 2019.

[29] P. Duan, J. Lai, J. Kang, X. Kang, P. Ghamisi, and S. Li, "Texture-aware total variation-based removal of sun glint in hyperspectral images," *ISPRS J. Photogrammetry Remote Sens.*, vol. 166, pp. 359–372, 2020.

[30] A. Riaza, J. Buzzi, E. Garcia-Melendez, B. Del Moral, V. Carrere, and R. Richter, "Monitoring salt crusts on an AMD contaminated coastal wetland using hyperspectral hyperion data (Estuary of the River Odiel, SW Spain)," *Int. J. Remote Sens.*, vol. 38, nos. 11/12, pp. 3735–3762, Mar. 2017.

[31] H. Duan, S. Xia, M. V. Jackson, N. Zhao, and J. Shi, "Identifying new sites of significance to waterbirds conservation and their habitat modification in the Yellow and Bohai Seas in China," *Global Ecol. Conservation*, vol. 22, Jun. 2020, Art. no. e01031.

[32] K. R. Turpie, V. V. Klemas, K. Byrd, M. Kelly, and Y. H. Jo, "Prospective HyspIRI global observations of tidal wetlands," *Remote Sens. Environ.*, vol. 167, pp. 206–217, Sep. 2015.

[33] H. A. Aboulela, R. A. Bantan, and R. A. Zeineldin, "Evaluating and predicting changes occurring on the coastlines of Jeddah city using satellite images," *Arabian J. Sci. Eng.*, vol. 45, no. 1, pp. 327–339, Mar. 2020.

[34] Z. Zifei and J. Tao, "A recognition method of wetland vegetation using the HICO hyperspectral image in Yellow River Estuary," *Beijing Surveying Mapping*, 2018.

[35] H. Lee and H. Kwon, "Going deeper with contextual CNN for hyperspectral image classification," *IEEE Trans. Image Process.*, vol. 26, no. 10, pp. 4843–4855, Oct. 2017.

[36] B. Sun, X. Kang, S. Li, and J. A. Benediktsson, "Random-walker-based collaborative learning for hyperspectral image classification," *IEEE Trans. Geosci. Remote Sens.*, vol. 55, no. 1, pp. 212–222, Jan. 2017.

[37] H. Su, Y. Yu, Q. Du, and P. Du, "Ensemble learning for hyperspectral image classification using tangent collaborative representation," *IEEE Trans. Geosci. Remote Sens.*, vol. 58, no. 6, pp. 3778–3790, Jun. 2020.

[38] D. Hong, L. Gao, J. Yao, B. Zhang, A. Plaza, and J. Chanussot, "Graph convolutional networks for hyperspectral image classification," *IEEE Trans. Geosci. Remote Sens.*, to be published.

[39] I. Dronova, "Object-based image analysis in wetland research: A review," *Remote Sens.*, vol. 7, no. 5, pp. 6380–6413, May 2015.

[40] D. Stratoulias, H. Balzter, A. Zlinszky, and V. R. Toth, "A comparison of airborne hyperspectral-based classifications of emergent wetland vegetation at Lake Balaton, Hungary," *Int. J. Remote Sens.*, vol. 39, no. 17, pp. 5689–5715, May 2018.

[41] D. Hong, L. Gao, N. Yokoya, J. Yao, and B. Zhang, "More diverse means better: Multimodal deep learning meets remote sensing imagery classification," *IEEE Trans. Geosci. Remote Sens.*, to be published.

[42] M. Michael, H. Claudia, S. Julien, W. Rebecca, and R. Edwards, "High-latitude wetland mapping using multidate and multisensor earth observation data: A case study in the northwest territories," *J. Appl. Remote Sens.*, vol. 14, no. 3, Aug. 2020, Art. no. 034511.

[43] A. Larocque, B. Leblon, R. Woodward, and L. Bourgeau-Chavez, "Wetland mapping in New Brunswick, Canada with LANDSAT5-TM, Alos-Palsar, and RADARSAT-2 Imagery," *ISPRS Ann. Photogrammetry, Remote Sens. Spatial Inf. Sci.*, vol. 3, no. 1, pp. 301–308, Jun. 2020.

[44] S. T. Seydi, M. Hasanlou, and M. Amani, "A new end-to-end multi-dimensional CNN framework for land cover/land use change detection in multi-source remote sensing datasets," *Remote Sens.*, vol. 12, no. 12, Jun. 2020, Art. no. 2010.

[45] M. Amani, B. Salehi, S. Mandavi, and B. Brisco, "Spectral analysis of wetlands using multi-source optical satellite imagery," *ISPRS J. Photogrammetry Remote Sens.*, vol. 114, pp. 119–136, Oct. 2018.

[46] R. Jahncke, B. Leblon, P. Bush, and A. Larocque, "Mapping wetlands in Nova Scotia with multi-beam RADARSAT-2 Polarimetric SAR, optical satellite imagery, and Lidar data," *Int. J. Appl. Earth Observ. Geoinf.*, vol. 68, pp. 139–156, 2018.

[47] X. Xu, W. Li, Q. Ran, Q. Du, and B. Zhang, "Multisource remote sensing data classification based on convolutional neural network," *IEEE Trans. Geosci. Remote Sens.*, vol. 56, no. 2, pp. 937–949, Feb. 2018.

[48] X. Zhao, T. Ran, W. Li, H. Li, W. Liao, and W. Philips, "Joint classification of hyperspectral and LiDAR data using hierarchical random walk and deep CNN architecture," *IEEE Trans. Geosci. Remote Sens.*, vol. 58, no. 10, pp. 7355–7370, Oct. 2020.

[49] S. L. Ozesmi and M. E. Bauer, "Satellite remote sensing of wetlands," *Wetlands Ecol. Manage.*, vol. 10, no. 5, pp. 381–402, Jun. 2002.

[50] K. S. Schmidt, A. K. Skidmore, E. H. Kloosterman, H. V. Oosten, L. Kumar, and J. A. M. Janssen, "Mapping coastal vegetation using an expert system and hyperspectral imagery," *Photogrammetric Eng. Remote Sens.*, vol. 70, no. 6, pp. 703–716, Jun. 2004.

[51] K. Tuxen *et al.*, "Mapping changes in tidal wetland vegetation composition and pattern across a salinity gradient using high spatial resolution imagery," *Wetlands Ecol. Manage.*, vol. 19, no. 2, pp. 141–157, 2011.

[52] A. O. Onojeghuo and A. R. Onojeghuo, "Object-based habitat mapping using very high spatial resolution multispectral and hyperspectral imagery with LiDAR data," *Int. J. Appl. Earth Observ. Geoinf.*, vol. 59, pp. 79–91, 2017.

[53] T. Liu and A. Abd-Elrahman, "Deep convolutional neural network training enrichment using multi-view object-based analysis of unmanned aerial systems imagery for wetlands classification," *ISPRS J. Photogrammetry Remote Sens.*, vol. 139, pp. 154–170, May. 2018.

[54] E. Belluco *et al.*, "Mapping salt-marsh vegetation by multispectral and hyperspectral remote sensing," *Remote Sens. Environ.*, vol. 105, no. 1, pp. 54–67, Jun. 2006.

[55] J. Wen, Y. Xu, Z. Li, Z. Ma, and Y. Xu, "Inter-class sparsity based discriminative least square regression," *Neural Netw.*, vol. 102, no. 2, pp. 36–47, Feb. 2018.

[56] Y. Xu, X. Fang, Q. Zhu, Y. Chen, J. You, and H. Liu, "Modified minimum squared error algorithm for robust classification and face recognition experiments," *Neurocomputing*, vol. 135, no. 5, pp. 253–261, Jul. 2014.

[57] Z. Lin, M. Chen, and Y. Ma, "The augmented lagrange multiplier method for exact recovery of corrupted low-rank matrices," 2010, *arXiv:1009.5055*.

[58] J. Yang and X. Yuan, "Linearized augmented lagrangian and alternating direction methods for nuclear norm minimization," *Math. Comput.*, vol. 82, no. 281, pp. 301–329, Mar. 2013.

[59] Y. Chen, H. Jiang, C. Li, X. Jia, and P. Ghamisi, "Deep feature extraction and classification of hyperspectral images based on convolutional neural networks," *IEEE Trans. Geosci. Remote Sens.*, vol. 54, no. 10, pp. 6232–6251, Oct. 2016.

[60] Y. Xu, L. Zhang, B. Du, and F. Zhang, "Spectral–Spatial unified networks for hyperspectral image classification," *IEEE Trans. Geosci. Remote Sens.*, vol. 56, no. 10, pp. 5893–5909, Mar. 2018.

[61] W. Zhao and S. Du, "Spectral-spatial feature extraction for hyperspectral image classification: A dimension reduction and deep learning approach," *IEEE Trans. Geosci. Remote Sens.*, vol. 54, no. 8, pp. 4544–4554, Aug. 2016.

[62] S. Santurkar, D. Tsipras, A. Ilyas, and A. Madry, "How does batch normalization help optimization?," in *Proc. Int. Conf. Neural Inf. Process. Syst.*, 2018, pp. 2483–2493.

[63] X. Li, W. Li, X. Xu, and Q. Du, "CascadeNet: Modified ResNet with cascade blocks," in *Proc. 24th Int. Conf. Pattern Recognit.*, Aug. 2018, pp. 483–488.

[64] C. Liu, M. Zhang, W. Li, W. Sun, and R. Tao, "Convolutional neural network for coastal wetland classification in hyperspectral image," in *Proc. IEEE Int. Geosci. Remote Sens. Symp.*, 2020.

[65] J. Yosinski, J. Clune, Y. Bengio, and H. Lipson, "How transferable are features in deep neural networks?," in *Proc. Int. Conf. Neural Inf. Process. Syst.*, 2014, pp. 3320–3328.

[66] Z. Zang, X. Zou, Q. Song, and Y. Yao, "Analysis of the spatiotemporal correlation between vegetation pattern and human activity intensity in Yancheng coastal wetland, China 1," *Coastal Environ. Changes under Increasing Anthropogenic Impacts*, vol. 2, no. 1, pp. 87–100, Jun. 2019.

[67] K. Shang, Y. Xie, and H. Wei, "Study on sophisticated vegetation classification for AHSI/GF-5 remote sensing data," *Proc. SPIE*, vol. 11432, 2020, Art. no. 114321A.

[68] Z. Ghassabi, J. Shanbehzadeh, A. Sedaghat, and E. Fatemizadeh, "An efficient approach for robust multimodal retinal image registration based on UR-SIFT features and PIIFD descriptors," *EURASIP J. Image Video Process.*, vol. 25, no. 2013, pp. 1–16, Jan. 2013.

[69] I. Naseem, R. Togneri, and M. Bennamoun, "Linear regression for face recognition," *IEEE Trans. Pattern Anal. Mach. Intell.*, vol. 32, no. 11, pp. 2106–2112, Nov. 2010.

[70] X. Sun, Q. Qu, N. M. Nasrabadi, and T. D. Tran, "Structured priors for sparse-representation-based hyperspectral image classification," *IEEE Geosci. Remote Sens. Lett.*, vol. 11, no. 7, pp. 1235–1239, Jul. 2014.

[71] W. Li, Q. Du, and M. Xiong, "Kernel collaborative representation with Tikhonov regularization for hyperspectral image classification," *IEEE Geoence Remote Sens. Lett.*, vol. 12, no. 1, pp. 48–52, Jan. 2015.

[72] C.-W. Hsu, C.-C. Chang, and C.-J. Lin, "A practical guide to support vector classification," Dept. Comput. Sci. Inf. Eng., National Taiwan University, Taipei, Taiwan, May 2003. [Online]. Available: www.csie.ntu.edu.tw/~cjlin/papers/guide/guide.pdf

[73] W. Li, C. Chen, H. Su, and Q. Du, "Local binary patterns and extreme learning machine for hyperspectral imagery classification," *IEEE Trans. Geosci. Remote Sens.*, vol. 53, no. 7, pp. 3681–3693, Jul. 2015.

Chang Liu (Student Member, IEEE) received the B.S. degree in electronic and information engineering from Hunan University, Changsha, China, in 2018. She is currently working toward the master's degree with the School of Information and Electronics, Beijing Institute of Technology, Beijing, China.

Her research interests include remote sensing image process and pattern recognition.

Ran Tao (Senior Member, IEEE) was born in Nanling County, Anhui Province, China, in 1964. He received the Ph.D. degree in electrical engineering from Harbin Institute of Technology, Harbin, China, in 1993. He has been a Professor at Beijing Institute of Technology, since 1999.

From March 2001 to April 2002, he was a Visiting Scholar at the University of Michigan, Ann Arbor.

He is currently a Professor with the School of Information and Electronics, Beijing Institute of Technology, Beijing, China. He was a Chief Professor of the Program for Changjiang Scholars and Innovative Research Team in University from 2010 to 2012. He has been a Chief Professor of the Creative Research Groups of the National Natural Science Foundation of China, since 2014. His research interests are in the areas of the fractional Fourier transform, time-frequency signal processing, and signal processing for radar and communications.

Prof. Tao was the recipient of the National Science Foundation of China for Distinguished Young Scholars, in 2006, and the First Prize of Science and Technology Progress, in 2006 and 2007, and the First Prize of Natural Science in 2013, both awarded by the Ministry of Education. He is currently the Vice Chair of the IEEE China Council and the URSI China Council.

Wei Li (Senior Member, IEEE) received the B.E. degree in telecommunications engineering from Xidian University, Xi'an, China, in 2007, the M.S. degree in information science and technology from Sun Yat-Sen University, Guangzhou, China, in 2009, and the Ph.D. degree in electrical and computer engineering from Mississippi State University, Starkville, MS, USA, in 2012.

He was a Postdoctoral Researcher with the University of California, Davis, CA, USA. He was a Professor with the College of Information Science and Technology, Beijing University of Chemical Technology, from 2013 to 2019. He is currently a Professor with the School of Information and Electronics, Beijing Institute of Technology, Beijing. His research interests include hyperspectral image analysis, pattern recognition, and data compression.

Dr. Li received the 2015 Best Reviewer Award from the IEEE Geoscience and Remote Sensing Society for his service for the IEEE JOURNAL OF SELECTED TOPICS IN APPLIED EARTH OBSERVATIONS AND REMOTE SENSING (JSTARS) and the Outstanding Paper Award at the IEEE International Workshop on Hyperspectral Image and Signal Processing: Evolution in Remote Sensing, 2019. He is an Associate Editor for the IEEE SIGNAL PROCESSING LETTERS and the IEEE JSTARS. He has served as the Guest Editor for special issue of the *Journal of Real-Time Image Processing*, *Remote Sensing*, and the IEEE JSTARS.

Mengmeng Zhang (Member, IEEE) received the B.S. degree in computer science and technology from the Qingdao University of Science and Technology, Qingdao, China, in 2014, and the Ph.D. degree in control science and engineering from the Beijing University of Chemical Technology, Beijing, China, in 2019.

She is currently a Postdoctoral Researcher with the School of Information and Electronics, Beijing Institute of Technology, Beijing. Her research interests include remote sensing image process and pattern recognition.

Qian Du (Fellow, IEEE) received the Ph.D. degree in electrical engineering from the University of Maryland, Baltimore, MD, USA, in 2000.

She is currently the Bobby Shackouls Professor with the Department of Electrical and Computer Engineering, Mississippi State University, Starkville, MS, USA. Her research interests include hyperspectral remote sensing image analysis and applications, pattern classification, data compression, and neural networks.

Dr. Du is a Fellow of the SPIE—International Society for Optics and Photonics. She received the 2010 Best Reviewer Award from the IEEE Geoscience and Remote Sensing Society. She was a Co-Chair of the Data Fusion Technical Committee of the IEEE Geoscience and Remote Sensing Society from 2009 to 2013 and the Chair of the Remote Sensing and Mapping Technical Committee of the International Association for Pattern Recognition from 2010 to 2014. She is the General Chair of the 4th IEEE GRSS Workshop on Hyperspectral Image and Signal Processing: Evolution in Remote Sensing, Shanghai, China, in 2012. She has served as an Associate Editor for the IEEE JOURNAL OF SELECTED TOPICS IN APPLIED EARTH OBSERVATIONS AND REMOTE SENSING, the *Journal of Applied Remote Sensing*, and the IEEE SIGNAL PROCESSING LETTERS. Since 2016, she has been the Editor-in-Chief of the IEEE JOURNAL OF SELECTED TOPICS IN APPLIED EARTH OBSERVATIONS AND REMOTE SENSING.

Weiwei Sun (Member, IEEE) received the B.S. degree in surveying and mapping and the Ph.D. degree in cartography and geographic information engineering from Tongji University, Shanghai, China in 2007 and 2013, respectively.

From 2011 to 2012, he was a Visiting Scholar with the Department of Applied Mathematics, University of Maryland College Park, College Park, MD, USA, where he worked with the famous Professor J. Benedetto to study on the dimensionality reduction of hyperspectral image. From 2014 to 2016, he was a Postdoctoral Researcher with the State Key Laboratory for Information Engineering in Surveying, Mapping and Remote Sensing, Wuhan University, Wuhan, China, where he studied intelligent processing in hyperspectral imagery. From 2017 to 2018, he was a Visiting Scholar with the Department of Electrical and Computer Engineering, Mississippi State University, Starkville, MS, USA. He is currently a Full Professor with Ningbo University, Ningbo, China. He has authored or coauthored more than 50 journal papers. His current research interests include hyperspectral image processing with manifold learning, anomaly detection, and target recognition of remote sensing imagery using compressive sensing.